First Observations of Solar Zenith Angle Modulation of Diurnal Tidal Structure in the MLT Region

Wen Yi[1,2,3], Jianyuan Wang[4], Xianghui Xue[1,3,5,6], Chengyun Yang[1,3], Iain M. Reid[7,8], Robert A. Vincent[7,8], Andrew MacKinnon[8], Damian J. Murphy[9], Njål Gulbrandsen[10], Masaki Tsutsumi[11], Baiqi Ning[12], Guozhu Li[12], Nicholas J. Mitchell[13,14], Tracy Moffat-Griffin[14], Toshitaka Tsuda[15], Haiying Li[16], Paulo P. Batista[17], Jianfei Wu[1,3], Tingdi Chen[1,3] , Xiankang Dou[1,6]

[1] School of Earth and Space Sciences, University of Science and Technology of China, Hefei, China
[2]State Key Laboratory of Environment Characteristics and Effects for Near-space, Beijing, China,
[3]National Field Observation and Research Station (Anhui Mengcheng) for Geophysics, University of Science and Technology of China, Hefei, China
[4]School of Microelectronics, Tianjin University, Tianjin, China,
[5] Hefei National Laboratory for the Physical Sciences at the Microscale, University of Science and Technology of China, Hefei, China
[6] Hefei National Laboratory, University of Science and Technology of China, Hefei, China
[7]ATRAD Pty Ltd., Underdale, South Australia, Australia,
[8]School of Physical Sciences, University of Adelaide, Adelaide, South Australia, Australia
[9]Australian Antarctic Division, Kingston, Tasmania, Australia
[10]Tromsø Geophysical Observatory, UiT – The Arctic University of Norway, Tromsø, Norway
[11]National Institute of Polar Research, Tachikawa, Japan
[12]Key Laboratory of Earth and Planetary Physics, Institute of Geology and Geophysics, Chinese Academy of Sciences, Beijing, China
[13]British Antarctic Survey, Cambridge, UK
[14]Department of Electronic & Electrical Engineering, The University of Bath, UK
[15]Research Institute for Sustainable Humanosphere (RISH), Kyoto University, Uji, Japan
[16]National Key Laboratory of Electromagnetic Wave Propagation, China Research Institute of Radiowave Propagation, Qingdao, China
[17]Heliophysics, Planetary Science and Aeronomy Division, National Institute for Space Research-INPE, São José dos Campos, SP, Brazil

Keywords: Diurnal Tides, Mesosphere and Low Thermosphere, Meteor Radar, Solar Zenith Angle

Corresponding author: Xianghui Xue (xuexh@ustc.edu.cn)

Abstract: A global climatology of diurnal tides in the mesosphere and lower thermosphere (MLT) is constructed using multiyear observations from fifteen meteor radars distributed worldwide. The results show that diurnal tidal amplitudes are strongest at low and mid-latitudes (10°–50° N/S), with peak values of about 60 m s^{-1} near 20°–30° N/S, and are comparatively weak near the Equator and at polar latitudes. The seasonal variations of the diurnal tide are characterized by maxima around the equinoxes and minima during the solstices. In addition to these global climatological features, we identify a clear modulation of the vertical structure of diurnal tidal amplitude and phase by seasonal variations in solar forcing, represented here by the solar zenith angle (SZA). This modulation is particularly evident at northern low and mid-latitudes, but is much weaker in the Southern Hemisphere. The hemispheric asymmetry suggests that the tidal response to solar forcing is not globally uniform. To further explore the possible cause of this asymmetry, we examine the meridional fluxes of zonal tidal momentum. The results suggest that background zonal winds can influence tidal propagation through filtering effects and momentum drag, thereby contributing to the observed hemispheric differences in tidal structure. These results provide new observational evidence for the coupling between solar forcing and diurnal tides in the MLT region and offer useful constraints for the evaluation of general circulation models. They also improve our understanding of tidal propagation and variability in the middle and upper atmosphere.

Introduction

The global wind field, temperature, density, and atmospheric composition of the mesosphere and lower thermosphere (MLT) region are strongly influenced by the vertical upward propagation of atmospheric (solar) tides that transport energy and momentum from the lower atmosphere to the middle and upper atmosphere (see, e.g., Forbes and Garrett, 1979; Forbes, 1995; Hagan and Forbes, 2002; Manson et al., 2004; Pancheva et al., 2014). Atmospheric tides in the MLT region are important components of the general circulation (Hagan and Forbes, 2002, Smith, 2012; Becker, 2017).

Ground-based and satellite techniques are widely used to observe atmospheric tides in the MLT region. Both of these techniques have their own advantages and limitations.

As tides are global-scale oscillations with periods that are harmonics of a solar day, satellite observations can capture both migrating and nonmigrating components (Hagan and Forbes, 2002; Manson et al., 2004; Oberheide et al., 2006; Wu et al., 2008a, 2008b; Mukhtarov et al., 2009; Xu et al., 2009; Pancheva et al., 2009, 2010; and the references therein). However, the limitations of satellite techniques are that their inclination precessing orbits basically take dozens of days to cover the whole day in local time. For example, the thermosphere, ionosphere, mesosphere energetics, and dynamics (TIMED) satellite needs 60 days to cover 24-hour measurements, so observations based on satellite techniques can usually provide the climatology of the slowly varying global-scale migrating and nonmigrating tides (Xu et al., 2009; Pancheva et al., 2009), but they are not well suited for investigating short-term variability in regional tides.

In addition to space-based observations, an advantage of ground-based techniques, such as meteor radar (MR) and medium frequency (MF) radar, is high temporal resolution of MLT tides, which in the last few decades have been successfully used for investigating the short-term variability and seasonal, intraseasonal and interannual variations in tides, as well as their long-term trend changes at various geographic locations (e.g., Manson et al., 1999, 2002, 2004; Jacobi et al., 1999; Riggin et al., 1999; Vincent et al., 1998; Mitchell et al., 2002; Pancheva et al., 2020; Yi et al., 2019, 2023; Stober et al., 2021a; Hindley et al., 2022; Wang et al., 2022; Zhou et al., 2022). The obvious limitation of a single station is its inability to resolve the global-scale oscillation of tides and extract migrating and nonmigrating tides.

To achieve the decomposition of tidal components, a few studies have used the longitudinal distribution of MRs and MFs at particular latitudes to resolve migrating and nonmigrating tidal components (e.g., Murphy, 2003; Murphy et al., 2006; He et al., 2018; He and Chau, 2019; Liu et al., 2020; Wang et al., 2022). However, in the last few decades, numerous studies have investigated mesospheric tides, which were often limited to a single station or particular latitudes (e.g., Manson et al., 2002; Davis et al., 2013; Stober et al., 2021a; 2021b; and the references therein). Therefore, the global picture of mesospheric tides observed by ground-based radars is still sparse.

Diurnal tides exhibit variability across a wide range of timescales, from days to years, primarily driven by two mechanisms: (1) variability in tropospheric and stratospheric tidal forcing (Zhang et al., 2010; Lieberman et al., 2007), and (2) amplitude modulation through interactions with the mean flow, planetary waves, and gravity waves (McLandress, 2002a, 2002b; Becker, 2017). Long-term variations in diurnal tides are further influenced by seasonal cycles, interannual phenomena such as the El Niño–Southern Oscillation (ENSO), the quasi-biennial oscillation (QBO), and the 11-year solar cycle. These factors affect both the generation and vertical propagation of tides by modulating tropospheric heating and background wind structures (Vincent et al., 1998; Lieberman et al., 2007; Hindley et al., 2022; Ramesh et al., 2024; Sheng et al., 2025).

The fifteen meteor radars used in this study provide extensive ground-based sampling of diurnal tides across both hemispheres. Although the network is not uniformly distributed in latitude and longitude, with several Northern Hemisphere low- and midlatitude stations concentrated in East Asia, it enables a broad characterization of the seasonal and vertical structures of locally observed diurnal tides. Here, we investigate the amplitude and phase variations of diurnal tides using multiyear observations from these fifteen meteor radars. Our results show that seasonal variations in solar forcing, represented by the solar zenith angle (SZA), are associated with systematic changes in the vertical amplitude and phase structures of locally observed diurnal tides. In addition, using horizontal wind measurements, we examine the coupling between tides and the background mean flow and discuss its possible role in shaping tidal amplitude, phase, and vertical structure. These findings provide new observational evidence that solar-forcing-related seasonal variations are reflected in the vertical structures of diurnal tides in the MLT region.

2. Data and Method

In this study, hourly horizontal wind data from fifteen meteor radars (MRs) are used. The locations of the stations and their abbreviations are shown in Figure 1, while their geographic coordinates, operating frequencies, peak powers, and observational periods are summarized in Table 1. The meteor radars used in this study were manufactured either by ATRAD Ltd. (Holdsworth et al., 2004) or Genesis Ltd. (Hocking et al., 2001), and have broadly similar designs and operating principles. The DVMR, BPMR, DWMR, FKMR, KMMR, WHMR, BJMR, MCMR, MHMR, TRMR, and SVMR, manufactured by ATRAD Ltd., provide temporal and vertical resolutions of 1 h and 2 km, respectively. The KTMR, ASSMR, ALOMR, and KEPMR, manufactured by Genesis Ltd., provide temporal and vertical resolutions of 1 h and 3 km, respectively. The ALOMR data used in this study were obtained from the earlier SKiYMET meteor radar operated near the Andes Lidar Observatory during 2009–2014 (Liu and Franke, 2020), rather than from the ATRAD-based multistatic CONDOR system deployed in the region since 2019 (Stober et al., 2022). For consistency in the tidal analysis, the horizontal wind data were analyzed at 2-km altitude intervals over the 80–100 km range. Reid et al. (2018) and Zeng et al. (2022) conducted collocated meteor-radar comparison campaigns at Davis Station in Antarctica and Kunming at low latitudes, respectively, and provided detailed assessments of meteor-radar wind performance and measurement uncertainties.

Table 1. Main operation parameters, geographic coordinates and observational time periods for the meteor radars used in this study.

	Meteor radars	Geographic coordinates	Frequency	Peak Power	Included date range	Approx. Years
Southern Hemisphere (SH)	Davis (DVMR)	68.6°S, 77.9°E	33.2 MHz	7.5 kW	2005-2024	20
	King Edward Point (KEPMR)	54.3° S, 36.5°W	35.2 MHz	7.5 kW	2016-2020	5
	Buckland Park (BPMR)	34.6°S, 138.5°E	55 MHz	40 kW	2016-2021	5
	Andes Lidar Observatory (ALOMR)	30.3°S, 70.7°W	35.2 MHz	7.5 kW	2009-2013	5
	Darwin (DWMR)	12.3°S, 130.8°E	33.2 MHz	7.5 kW	2006-2014	8
	Ascension Island	7.9°S, 14.4° W	43.5 MHz	12 kW	2002-2011	10

	(ASSMR)					
	Kototabang (KTMR)	0.2°S, 100.3°E	37.7 MHz	12 kW	2003-2017	14
Northern Hemisphere (NH)	Fuke (FKMR)	19.5°N, 109.1°E	38.9 MHz	20 kW	2015-2020	6
	Kunming (KMMR)	25.6°N 103.8°E	37.5 MHz	20 kW	2011-2016	5
	Wuhan (WHMR)	30.5°N, 114.4°E	38.9 MHz	20 kW	2012-2024	13
	Mengcheng (MCMR)	33.4°N, 116.1°E	38.9 MHz	20 kW	2014-2024	11
	Beijing (BJMR)	40.3°N, 116.2°E	38.9 MHz	7.5 kW	2012-2023	12
	Mohe (MHMR)	53.5°N, 122.3°E	38.9 MHz	20 kW	2012-2024	13
	Tromsø (TRMR)	69.6°N, 19.2°E	30.3 MHz	7.5 kW	2004-2023	20
	Svalbard (SVMR)	78.2°N, 16.0°E	31 MHz	7.5 kW	2004-2023	20

To extract the tidal components observed by the meteor radars, we calculate the amplitude and phase of tidal components. The tidal analysis involves harmonics fitted to the hourly mean zonal and meridional winds. The fitting function is given by

$$y(t) = \bar{y}(t) + \sum_{i=1}^{3} A_i \sin\left(\frac{2\pi i}{24} t + \emptyset_i\right), \quad (1)$$

where $y(t)$ is the wind measurement, $\bar{y}(t)$ is the prevailing component, and A_i and $\emptyset_i$ represent the amplitude and phase, respectively. The tidal components with periods of 24 h, 12 h and 8 h represent the diurnal, semidiurnal and terdiurnal tides, respectively. As shown in Figure A1 in the Appendix A, we tested multiple fitting-window lengths (5, 7, and 11 days). Although the 11-day window produces somewhat stronger smoothing of short-term variability than the 5- and 7-day windows, the main seasonal variations in diurnal tidal amplitudes and phases remain broadly consistent among the three window lengths. Therefore, the influence of fitting-window length is relatively small for the seasonal-scale variability emphasized in this study, although shorter-term tidal variations are more sensitive to the choice of window. Based on this assessment, we adopted a 7-day window with a 1-day step as a compromise between temporal resolution and fitting stability.

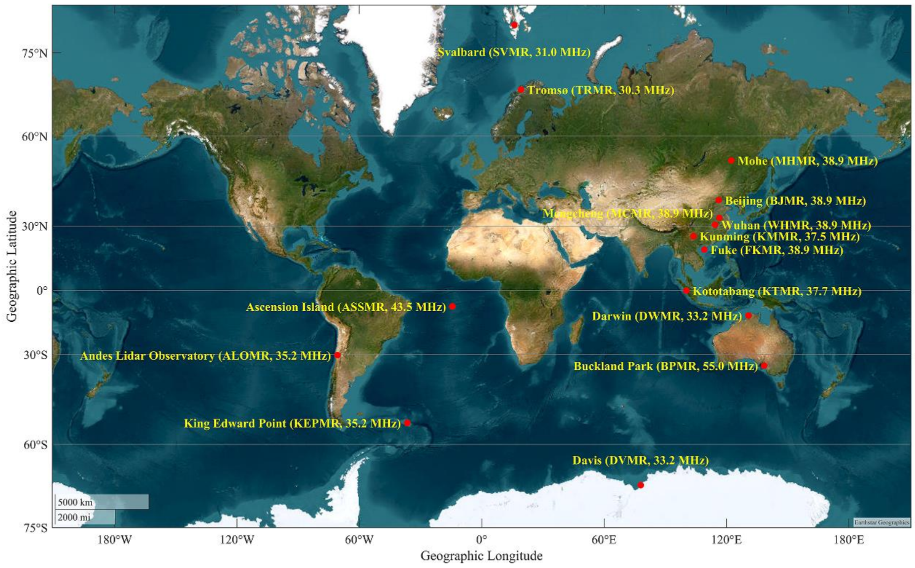

Figure 1. The locations of the Davis Station (DVMR, 68.6°S, 77.9°E), King Edward Point Station (KEPMR, 54° S, 36° W), Buckland Park (BPMR, 34.6°S, 138.5°E), Andes Lidar Observatory (ALOMR, 30.3° S, 70.7° W), Darwin (DWMR, 12.3° S, 130.5° E), Ascension Island (ASSMR, 7.9° S, 14.4° W), Kototabang (KTMR, 0.2°S, 100.3°E), Fuke (FKMR, 19.5°N, 109.1°E), Kunming (KMMR, 25.6°N, 103.8°E), Wuhan (WHMR, 30.6° N, 114.4° E), Mengcheng (MCMR, 33.4° N, 116.5° E), Beijing (BJMR, 40.3° N, 116.2° E), Mohe (MHMR, 53.5° N, 122.3° E), Tromsø (TRMR, 69.6° N, 19.2° E), and Svalbard (SVMR, 78.2°N, 16°E).

The DT results are based on radar measurements with varying lengths of observational records. Some radars, such as ALOMR, KMMR, and KEPMR, have only 5 years of data, whereas others, such as DVMR and TRMR, have up to 20 years. These differences in record length and observational period may influence the estimated mean tidal amplitudes and phases because diurnal tides also exhibit considerable interannual variability. To assess the sensitivity of the climatological results to record length, Figures A2 and A3 compare DT amplitudes and phases derived from the long-term DVMR record with those obtained from a 5-year subset. Although some differences in magnitude are evident, the principal seasonal–altitude structures remain very similar, suggesting that the main climatological features presented in this study are relatively robust.

3. Results

3.1 Seasonal Variation of Global Diurnal Tides

Figure 2 presents the seasonal–altitude structures of monthly mean diurnal tidal (DT) amplitudes and phases in zonal and meridional winds from the southern to northern polar regions. At polar latitudes, DT amplitudes from SVMR, TRMR, and DVMR show annual variation, peaking in summer and weakening in winter, with similar zonal and meridional patterns. In general, the DT amplitude during summer in both polar regions shows a relatively weak enhancement at lower altitudes below 84 km, reaching values up to 10 m/s, and a strong enhancement at higher altitudes above 96 km, reaching values up to 20 m/s. Stober et al. (2021b) reported that the DT amplitudes observed by the McMurdo meteor radar (77.8°S) at higher polar latitudes in the SH show stronger enhancements during summer in zonal components and have semiannual enhancements during March-May (autumn) and September-November (spring) in meridional components, which presents a different seasonal pattern of diurnal tides to the DVMR observations.

At higher northern midlatitudes, the zonal and meridional DT amplitudes observed by the MHMR show similar seasonal patterns to the high-latitude TRMR observations, reaching their maximum during summer with values up to 10 m/s. At southern higher midlatitudes, the KEPMR zonal DT amplitudes are very weak and show two weak enhancements in March (autumn) and September (spring), reaching values up to 10 m/s. The KEPMR meridional DT amplitudes are much stronger than those of the zonal component, which shows enhancements above 96 km with a maximum near the spring equinox, reaching values up to 20 m/s (e.g., Hindley et al., 2022). Although MHMR and KEPMR are located at geographically conjugate higher mid-latitudes, the diurnal tides observed at the two stations show a clear seasonal asymmetry.

The DT amplitudes observed by the BJMR, MCMR, and WHMR from 40°N to 30°N at northern midlatitudes generally exhibit a similar seasonal pattern. They show a first enhancement near the spring equinox and a second enhancement around the autumn equinox. The DT amplitudes of the zonal components observed by the BJMR and MCMR, reaching values up to 30 m/s and 45 m/s, respectively, are stronger than the values of the meridional component, reaching up to 25 m/s and 35 m/s, respectively. At lower midlatitudes near 30° N, the WHMR zonal and meridional DT amplitudes are generally equal, reaching values up to 50 m/s.

At southern midlatitudes near 30°S, the DT amplitude observed by ALOMR exhibits two significant enhancements that appear near the spring and autumn equinoxes. At higher latitudes, the BPMR DT amplitude exhibits a strong enhancement near the autumn equinox and a second enhancement in the later autumn equinox. However, the seasonal morphology of the diurnal tides at the approximately conjugate lower mid-latitude stations ALOMR (30.3°S) and WHMR (30.2°N) shows a clear hemispheric asymmetry. Both exhibit enhanced amplitudes during February–March, but this period corresponds to autumn at ALOMR and spring at WHMR.

At northern low latitudes, the zonal and meridional DT amplitudes observed by the KMMR and FKMR exhibit two significant enhancements that appear in February-March and September-November. Different from the midlatitudes, the meridional DT amplitudes at low latitudes are stronger than those of the zonal component. Deepa et al. (2008) reported that the zonal and meridional DT amplitudes observed in the Trivandrum (8.5°N) meteor radar reach maxima during autumn (August–November) and spring (March), and meridional amplitudes are stronger than zonal amplitudes, which are generally similar to the FKMR (19.5°N) observations.

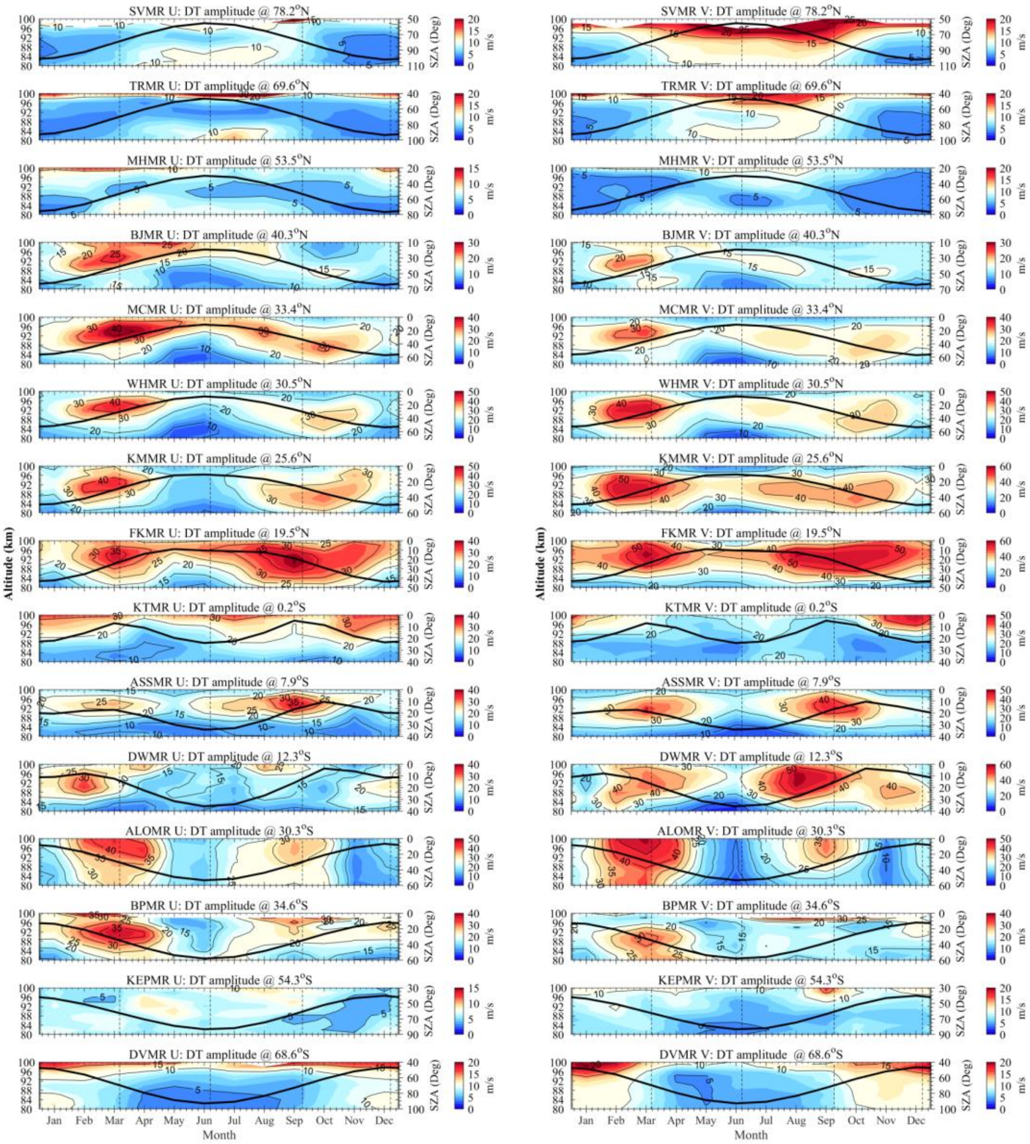

Figure 2. Monthly mean amplitudes of composite zonal (left column) and meridional (right column) diurnal tidal (DT) components derived from fifteen meteor radars. Note that the colorbar scales differ among panels. The black lines represent the solar zenith angle at local noon (1200 LT), corresponding to the right axes. Vertical black dashed lines indicate the spring and autumn equinoxes, as well as the summer and winter solstices.

At southern low latitudes, zonal DT amplitudes observed by the DWMR exhibit strong enhancement in summer (February) and weaker enhancement in spring (September). The meridional DT amplitudes show two peaks—one in spring (September) and another during March–April. Zonal amplitudes from the ASSMR display semiannual variations, peaking near the equinoxes (September and March) (e.g., Davis et al., 2013). Meridional DT amplitudes from both DWMR and ASSMR show similar semiannual patterns, with peak values reaching ~60 m/s in DWMR data. Kishore Kumar et al. (2014) also reported semiannual variations over Cachoeira Paulista (22°S), with meridional and zonal amplitude peaks of 55 m/s and 45 m/s, respectively—similar to ALOMR observations at 30°S. At the equator, KTMR data show three peaks: January–February, June–July, and November–December. These amplitudes increase with altitude, reaching ~40 m/s near 100 km.

Figure 3 presents the monthly mean phases of the zonal and meridional diurnal tides (DTs), defined as the time of the first positive maximum in the hourly wind measurements. Since the phases are calculated in local time, longitudinal differences among radars are eliminated. At high latitudes, SVMR and TRMR exhibit semiannual variations in both components, while DVMR displays annual variations, characterized by more stable phases and longer vertical wavelengths compared to SVMR and TRMR. At higher northern midlatitudes, the DT phases at MHMR resemble those at TRMR, with semiannual variation in the zonal component and annual variation in the meridional component. In contrast, KEPMR at southern midlatitudes shows semiannual variations in both components—differing from DVMR but similar to ALOMR and BPMR. The zonal DT phases at ALOMR exhibit weak annual variation, whereas the meridional phases are semiannual and more variable. For both BPMR and ALOMR, meridional vertical wavelengths are shorter in summer and longer in winter.

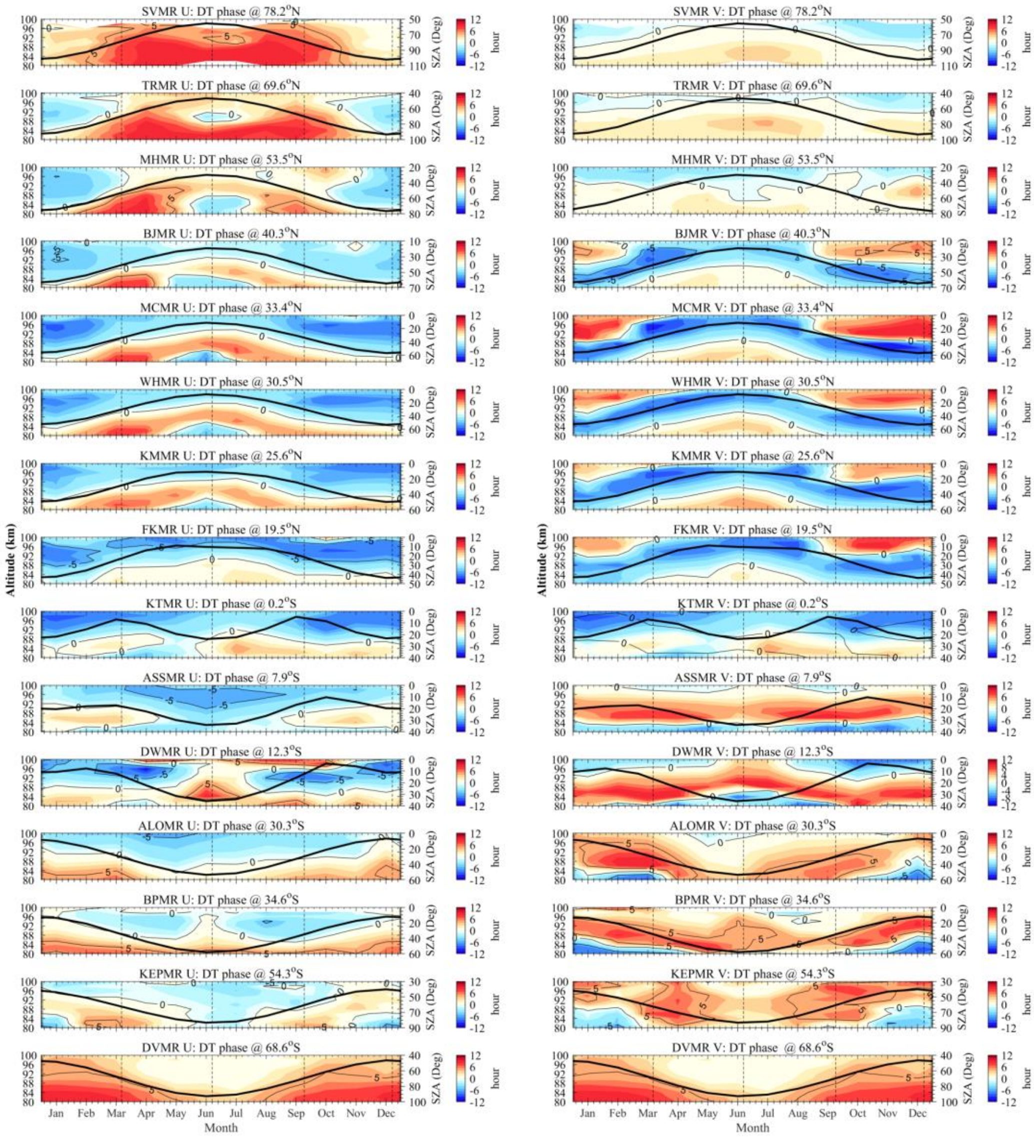

Figure 3. Same as Figure 2, but for the monthly mean phases of composite zonal (left column) and meridional (right column) diurnal tidal (DT) components.

The zonal and meridional DT phases observed by the BJMR, MCMR, WHMR, KMMR, and FKMR from middle to lower latitudes in the NH generally exhibit similar seasonal characteristics. Both zonal and meridional DT phases remain stable throughout the year and are indicative of upward propagating tides. Their diurnal tidal vertical wavelengths during summer and winter are generally longer than those during spring and autumn. Note that this behavior is consistent with the Hough-mode decomposition shown in Lieberman et al. (2003, their Fig. 9) for the migrating diurnal tide: the (1, 2) mode maximizes near the equinoxes and has a vertical wavelength of ~15 km, whereas the (1,

1) mode exhibits a weak annual cycle and a longer vertical wavelength. There are approximately 3-6/6-12 hour phase lags between the zonal and meridional components during summer/winter. In the SH low latitudes (KTMR, ASSMR, DWMR), DT phases are also stable with small seasonal changes but show clear zonal–meridional differences. At the equator, KTMR zonal wavelengths shorten near equinox and lengthen in winter and spring. The ASSMR zonal DT phases at SH lower latitudes show similar seasonal variations with KTMR.

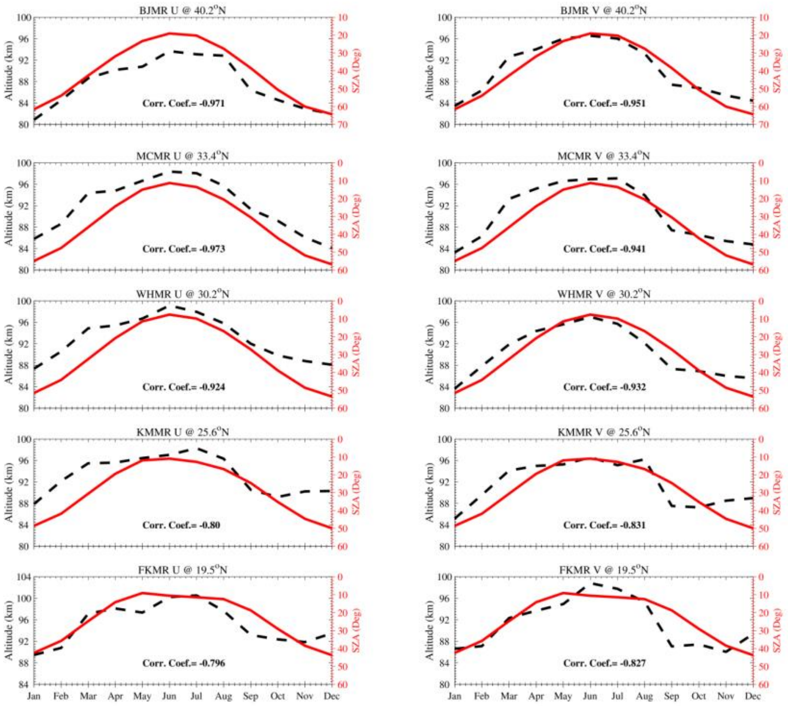

Figure 4. Comparison of the altitudes corresponding to zero phase of the zonal (left column) and meridional (right column) diurnal tides observed at Beijing, Mengcheng, Wuhan, Kunming, and Fuke with the solar zenith angle. The corresponding correlation coefficients are marked in each panel.

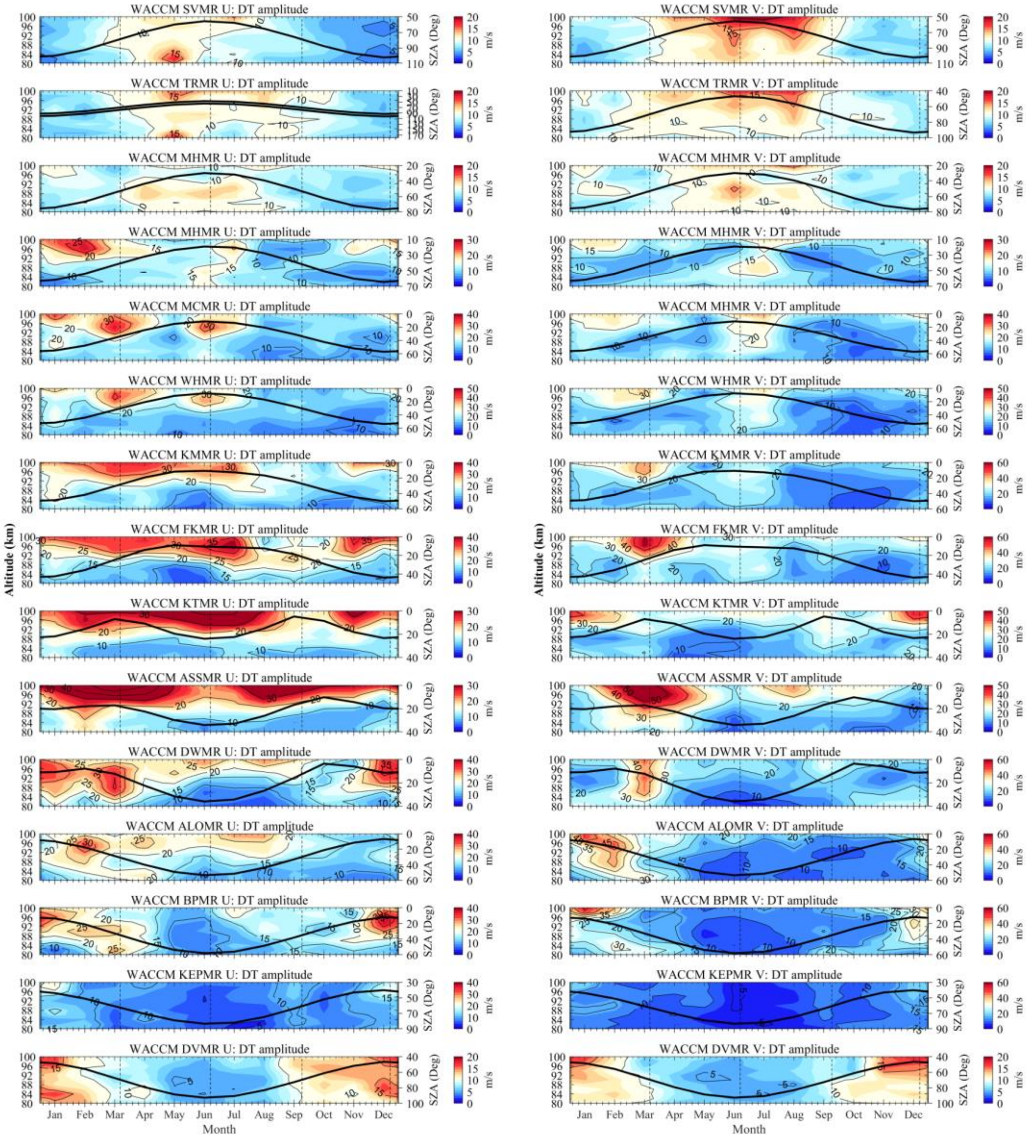

Figure 5. Same as Figure 2, but for the monthly mean amplitudes of composite zonal (left column) and meridional (right column) diurnal tidal (DT) components obtained from the SD-WACCM.

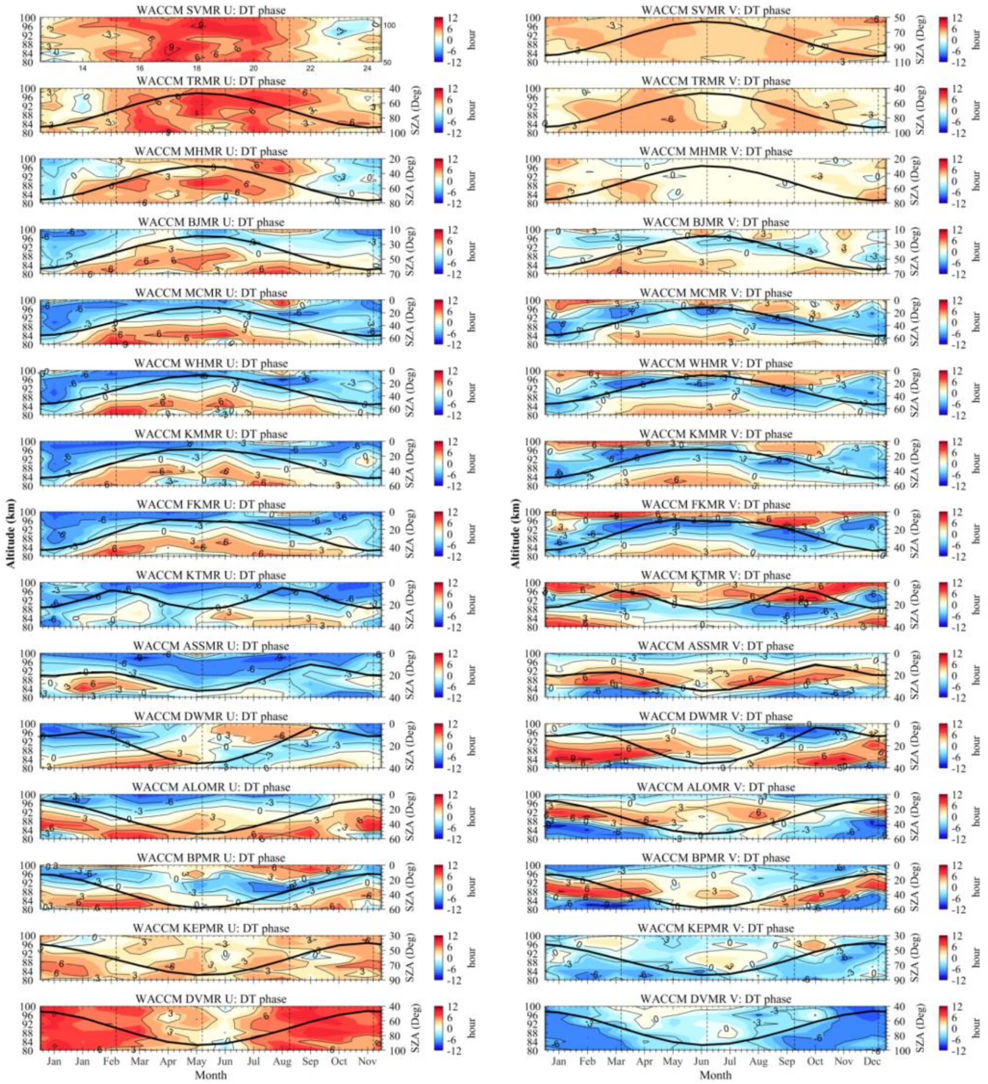

Figure 6. Same as Figure 3, but for the monthly mean phases of composite zonal (left column) and meridional (right column) diurnal tidal (DT) components obtained from the SD-WACCM.

3.2 Solar Zenith Angle Modulation of Seasonal Diurnal Tide Structures

Figure 2 also shows seasonal variations of solar zenith angle (SZA) at 12 LT over fifteen meteor radars. In this study, we adopt the SZA at local noon (12:00 LT) as a representative value (e.g., Liu et al., 2019), since it closely reflects the maximum daily solar heating and captures the dominant seasonal trend relevant for atmospheric tidal excitation.

A clear correspondence is observed between the seasonal variation in SZA and the altitude of the diurnal-tide amplitude maxima, particularly at northern midlatitudes

(BJMR, MCMR, and WHMR), and to a lesser extent at northern low latitudes (KMMR and FKMR). Near the equator, DT amplitudes at KTMR exhibit a semiannual variation that also appears to be linked to SZA. In the southern midlatitudes, the vertical variation of DT amplitudes at BPMR is also correlated with SZA, although the relationship is weaker compared to that in the Northern Hemisphere. Overall, the observations indicate that the seasonal variation in the altitude of the DT amplitude maxima is closely associated with the seasonal variation in SZA at several low- and midlatitude stations, with a clear hemispheric asymmetry in the strength of this relationship. As shown in Figure A4, the global semidiurnal tidal (SDT) amplitudes observed by the fifteen meteor radars do not show such SZA dependence.

Compared to the DT amplitudes, the seasonal variations of the DT phase shown in Figure 3 exhibit a stronger correspondence with seasonal changes in solar forcing, as represented by the noon SZA. This effect is most evident across lower and midlatitudes in the NH, particularly at BJMR, MCMR, WHMR, KMMR and FKMR. Figure 4 further compares the altitudes corresponding to zero phase of the zonal and meridional diurnal tides observed at BJMR, MCMR, WHMR, KMMR, and FKMR with the SZA. Strong correlations are found at the midlatitude stations BJMR, MCMR, and WHMR, while relatively high correlations are also evident at the lower-latitude stations KMMR and FKMR. These results provide quantitative support for a pronounced SZA-related seasonal modulation of the vertical structure of diurnal tides in the MLT region, consistent with an important solar-heating imprint on the observed tidal variability. Similar to the DT amplitudes, no clear correspondence between the DT phase and SZA is observed at the Southern Hemisphere stations, indicating a hemispheric asymmetry in the SZA-related seasonal variation of DT phase. As shown in Figure A5, the phases of the semidiurnal tide (SDT) exhibit no clear relationship with SZA, suggesting that the SZA-related seasonal signature identified for the diurnal tide is not evident in the SDT. As shown in Figures 5 and 6, we also computed the diurnal tidal (DT) amplitude and phase from hourly winds simulated by the specified-dynamics version of the Whole Atmosphere Community Climate Model (SD-WACCM), sampled at the meteor-radar locations. The simulation is nudged toward MERRA meteorological fields produced using the Goddard Earth Observing System Model, Version 5 (GEOS-5) data assimilation system (Rienecker et al., 2008). It employs a horizontal resolution of 1.9° latitude × 2.5° longitude and the high-vertical-resolution lev144 configuration with 144 vertical model levels, providing a vertical resolution of approximately 0.5 km in the MLT region (Zhou et al., 2022). In the specified-dynamics configuration, winds and temperatures in the lower atmosphere are constrained toward the reanalysis fields, while the model runs freely in the MLT region (Cen et al., 2022). Hourly zonal and meridional winds from the model are used in the present tidal analysis. SD-WACCM reproduces the seasonal variation of DT amplitudes at high latitudes, with maxima in summer and minima in winter (Stober et al., 2021a). However, at low and midlatitudes it fails to capture the seasonal behavior of the diurnal tides observed by the meteor radars used in this study, consistent with the findings of Zhou et al. (2022).

We further examine whether SD-WACCM can reproduce the seasonal variations in the vertical structures of DT amplitude and phase associated with variations in SZA. SD-WACCM generally does not reproduce the observed SZA-related features in DT amplitudes, whereas it largely captures the corresponding seasonal variations in DT phase at Northern Hemisphere midlatitudes. The discrepancies between the observations and SD-WACCM suggest that the excitation and evolution processes of diurnal tides in the mesosphere–lower thermosphere (MLT) region are still not fully understood.

3.3 Discussion on Hemispheric Differences in Diurnal Tide Modulation by Solar Zenith Angle

Figure 7 presents latitude–seasonal contour plots of the zonal and meridional diurnal tidal (DT) amplitudes at 86 and 92 km, derived from fifteen meteor radars. Across the mesopause region, both components generally maximize at ~20–30° N/S, consistent with direct global tidal wind measurements from TIMED/TIDI that show low-latitude DT wind maxima near ~20–30° and around ~90 km (e.g., Oberheide et al. 2006; Wu et al. 2008a, 2008b) and with multi-instrument tidal wind/temperature inferences from

Huang et al. (2006). Overall, the meridional DT amplitudes tend to be stronger than the zonal components. Seasonally, zonal diurnal tides typically peak around the equinoxes and reach minima near the solstices. The global structure indicates that DT amplitudes are largely characterized by semiannual variations, though annual and intraseasonal components are also present (e.g., Das et al., 2013; Yi et al., 2019; Guharay et al., 2021). It is important to note that the DTs observed by single-station meteor radars represent a combination of migrating and nonmigrating tides, which cannot be readily separated. In some cases, nonmigrating components may even dominate over the migrating ones (Forbes and Garrett, 1979). Migrating diurnal tides are primarily driven by solar infrared absorption by tropospheric water vapor and ultraviolet absorption by zonal-mean ozone in the stratosphere and lower mesosphere (Chapman and Lindzen, 1970; Forbes and Garrett, 1979; Lieberman et al., 2003).

In contrast, nonmigrating tides arise from more complex mechanisms, including zonally asymmetric thermal forcing (e.g., surface topography, localized heating, and longitudinal variations in solar heating) and nonlinear interactions with stationary planetary waves (Hagan and Forbes, 2002, 2003). Accurate modeling of these tides therefore requires consideration of a broad range of radiative, chemical, and dynamical processes, including the distributions of latent heating, ozone, and water vapor; background temperature and winds; molecular and eddy diffusivity; gravity-wave drag; and Newtonian cooling (Manson et al., 2002).

Accordingly, the correspondence between SZA and the locally observed DT structure should not be interpreted as a one-to-one response to direct solar heating. In this study, SZA is used primarily as an indicator of the seasonal variation in solar illumination. The observed SZA-related variations should therefore be regarded as a seasonal solar-forcing imprint on the locally observed composite diurnal tide, whose amplitudes and phases are further modified during propagation. Departures from this relationship may reflect contributions from zonally asymmetric heating, latent heating, topography, background circulation, and interactions with planetary and gravity waves.

In Figures 7e and 7f, we present the seasonal and latitudinal variations of surface net solar radiation and surface latent heat flux derived from the ERA5 reanalysis produced by the European Centre for Medium-Range Weather Forecasts (ECMWF; Hersbach et al., 2020). Monthly climatologies of these two ERA5 variables were used to characterize the seasonal variations in surface radiative and latent-heat forcing. As shown in Figure 7e, surface net solar radiation is strongly controlled by the seasonal variation in solar illumination, with larger values occurring in the summer hemisphere. The seasonal variation in surface latent heat flux, shown in Figure 7f, is strongly latitude dependent, with larger magnitudes at low and mid-latitudes and substantially weaker values at high latitudes. Latent heat flux tends to be stronger in the winter hemisphere than in the summer (Kubota et al., 2003; Zhang et al., 2018). These results suggest that the solar heating sources of tides are generally symmetric between hemispheres. However, this symmetry does not explain why the observed SZA modulation of diurnal tides occurs, implying that other factors such as background winds or dynamical interactions may be involved.

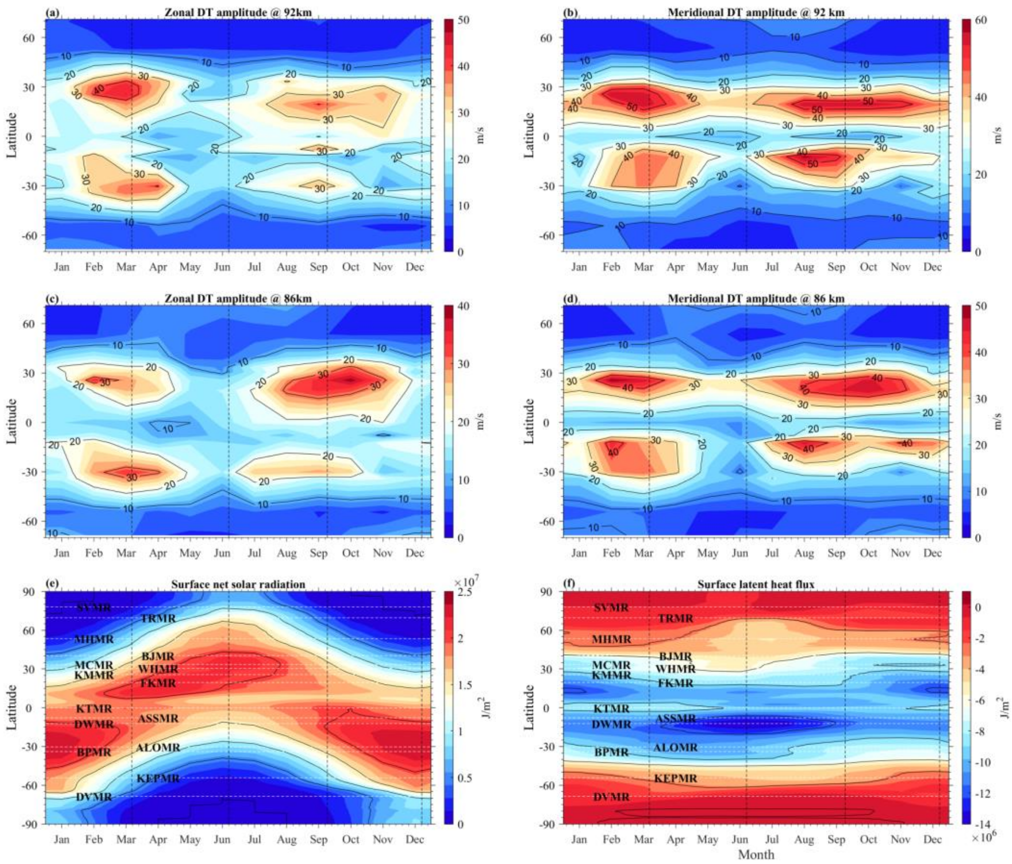

Figure 7. (a–d) Latitude–seasonal variations in the zonal and meridional diurnal tidal

amplitudes at 92 and 86 km derived from the fifteen meteor radars. (e–f) Surface net solar radiation and surface latent heat flux derived from the ERA5 reanalysis produced by the European Centre for Medium-Range Weather Forecasts (ECMWF). Note that the colorbar scales differ among panels.

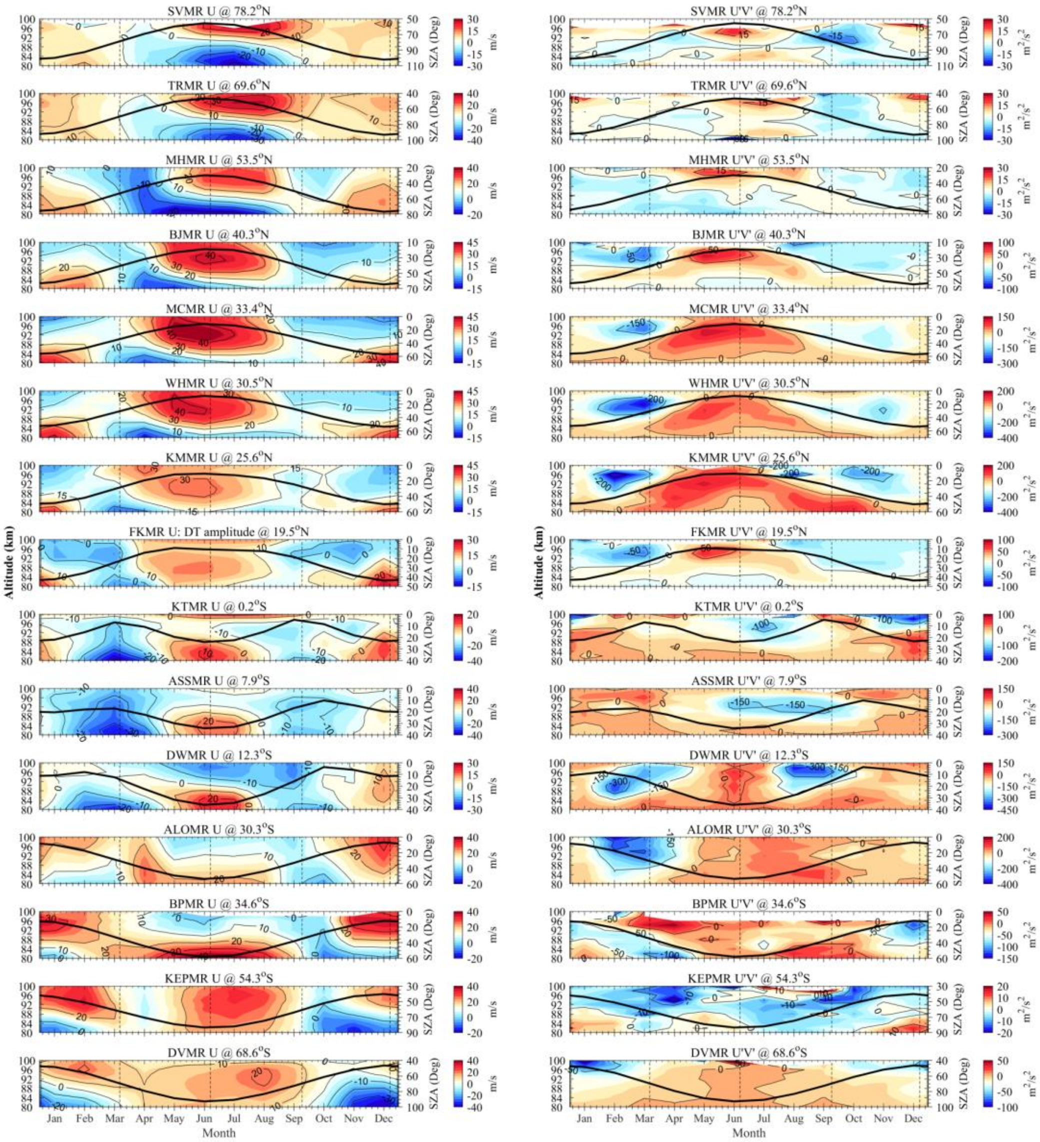

Figure 8. Comparison of background zonal wind (left column) and the meridional flux of tidal zonal momentum (right column) calculated by the fifteen meteor radars. Note that the colorbar scales differ among panels.. The black lines depict the solar zenith angle at 12 LT noon, corresponding to the right axes. The vertical black dashed lines depict the spring and autumn equinoxes and summer and winter solstices.

In addition to the excitation sources, the influence of background circulation on tides should also be considered. The background zonal mean flow can affect the upward propagation process of tides through Doppler effects, which alter the phase of diurnal tides in both zonal and meridional wind tidal components. Under ideal conditions, the zonal and meridional components of diurnal tides are approximately in quadrature, with a constant phase difference of 90°, resulting in negligible meridional flux of tidal zonal momentum ($u'v'$). However, variations in background zonal winds can modify the tidal phases through Doppler effects, thereby disrupting this orthogonality and producing nonzero $u'v'$. Therefore, the meridional flux of tidal zonal momentum provides a useful indicator for characterizing the interaction between background circulation and tides, as it reflects deviations from the ideal phase relationship between tidal wind components. The meridional flux of tidal zonal momentum can be derived using zonal and meridional wind tides, which is given as follows (Devara and Ahmed, 1986):

$$\overline{u'v'} = \frac{1}{2}\hat{u}\hat{v}cos(\phi_u - \phi_v) \quad (2)$$

where $\overline{u'v'}$ denotes the meridional flux of tidal zonal momentum; $\hat{u}$ and $\hat{v}$ represent the amplitudes of the zonal and meridional wind tides, respectively; ϕ_u and ϕ_v denote the phase of zonal wind tide and meridional tide, respectively.

Figure 8 presents the comparison between background zonal winds and the meridional flux of tidal zonal momentum calculated from the 15 meteor radars. It is noted that observations from BJMR, MCMR, WHMR, KMMR, and FKMR, located at mid-latitudes in the Northern Hemisphere, show that the background zonal wind reaches its maximum eastward intensity at the same altitude and month as the maximum eastward meridional flux of tidal zonal momentum. Since $u'v'$ approaches zero when the phase relationship between zonal and meridional tidal components remains close to quadrature, and vice versa, this suggests a potential relationship between strong eastward zonal winds and the departure of tidal components from quadrature.

The (1,1) Hough mode of zonal wind diurnal tides reaches maximum amplitude near 25° latitude, while the corresponding meridional wind component peaks around 20° latitude. Therefore, diurnal tides at mid-latitudes are mainly controlled by the (1,1) mode of migrating tides with westward propagating zonal wavenumber 1. When strong eastward background zonal winds prevail, the phase speed of the westward-propagating tides is opposite to the background flow. The Doppler effect induced by the opposing background wind increases the intrinsic frequency of the tides, which modifies the vertical and horizontal phase structures of the tidal components. As a result, the phase difference between the zonal and meridional tidal winds decreases from quadrature, thereby producing a significant positive $u'v'$ and enhancing the eastward meridional flux of tidal zonal momentum. The seasonal variation of background zonal winds may modify the phase structure of these tidal components in the mid-latitude region, leading to corresponding variations in tidal momentum flux. In the high- and low-latitude regions, this correspondence is disrupted due to the complexity of tidal modes and the altered seasonal variability of zonal winds. This could be one of the possible reasons for the relatively poor correlation between SZA and tidal activity in the high- and low-latitude regions.

However, in the southern hemisphere, the consistency between the eastward zonal wind and the positive diurnal tidal zonal momentum is only observed at BPMR although ALOMR is also located at mid-latitude in the southern hemisphere. This suggests that the possible mechanism at BPMR may resemble that in northern hemisphere mid-latitudes, while ALOMR exhibits distinct behavior. Although ALOMR and BPMR share similar latitudes, BPMR is situated in Australia, whereas ALOMR is located near the Andes Mountains in South America. Beyond the Doppler effects of the background flow on tides, gravity waves may also interact with tidal components (e.g., Liu and Hagan, 1998; Li et al., 2009; Stober et al., 2021a). The Andes Mountains near ALOMR generate strong topographic gravity waves with varying seasonal characteristics (e.g., Alexander and Teitelbaum, 2011; Cao et al., 2016; Randall et al., 2017; Llamedo et al., 2019), which could modify tidal amplitudes and phases, leading to deviations in the seasonal variations of tides from the SZA line.

4. Conclusion

In Section 3, we show the climatology of global diurnal tides in the MLT region observed by fifteen meteor radars, especially the modulation of mesospheric tides by solar heating, which can be briefly summarized as follows:

1. In general, the diurnal tides are strong at lower and middle latitudes (10-50°N/S), reaching maxima near 20-30°N/S with values of approximately 60 m/s, and are weak

at the equator and higher mid- and polar latitudes (higher than 50°N/S).

2. In terms of seasonal variation, the diurnal tides at lower and mid-latitudes generally reach maxima near equinoxes and have smaller amplitudes during summer and winter solstices. In the equatorial region, the diurnal tides show enhancements during January-February, June-August, and October-November. In the polar region, the diurnal tides show enhancements during summer and are weak during winter.

3. The seasonal evolution of the vertical structures of DTs exhibits a systematic relationship with solar illumination, represented by SZA, particularly at northern lower and midlatitudes. However, this relationship is weaker in the Southern Hemisphere, indicating a significant hemispheric asymmetry.

4. Global distributions of meridional fluxes of zonal tidal momentum highlight the critical role of background zonal winds in modulating tidal propagation. These winds can selectively filter tidal components and exert momentum forcing (or drag), thereby influencing both the amplitude and phase of the diurnal tide. This zonal wind–tide interaction is recognized as a primary mechanism contributing to the interhemispheric asymmetry observed in global tidal structures.

5. The comparison with SD-WACCM shows that the model reproduces some broad features of the observed seasonal diurnal-tide variability, particularly the seasonal amplitude variation at higher latitudes and part of the phase structure at Northern Hemisphere mid-latitudes. However, SD-WACCM does not fully capture the observed seasonal amplitude patterns at low and mid-latitudes and generally fails to reproduce the SZA-related modulation of the vertical amplitude structure. These model–observation differences demonstrate the value of the multi-station meteor-radar climatology as an observational constraint for evaluating and improving the representation of tidal excitation, propagation, and variability in whole-atmosphere models.

In conclusion, this study provides an unusually broad ground-based climatological perspective on locally observed diurnal tides using fifteen meteor radars distributed across both hemispheres. The resulting dataset offers a valuable observational benchmark for evaluating the seasonal and vertical structures of diurnal tides in atmospheric models, while the non-uniform station distribution should be considered when generalizing the inferred hemispheric differences to unsampled longitude sectors. The pronounced signatures of solar-heating-driven tides highlight persistent deficiencies in current models and underscore the need to better represent the underlying dynamical processes that link the lower atmosphere to the MLT region.

Appendix A: Comparison of Meteor Radar Tidal Estimations with Different Time Windows and Global Observations of the Semidiurnal Tide by Meteor Radars

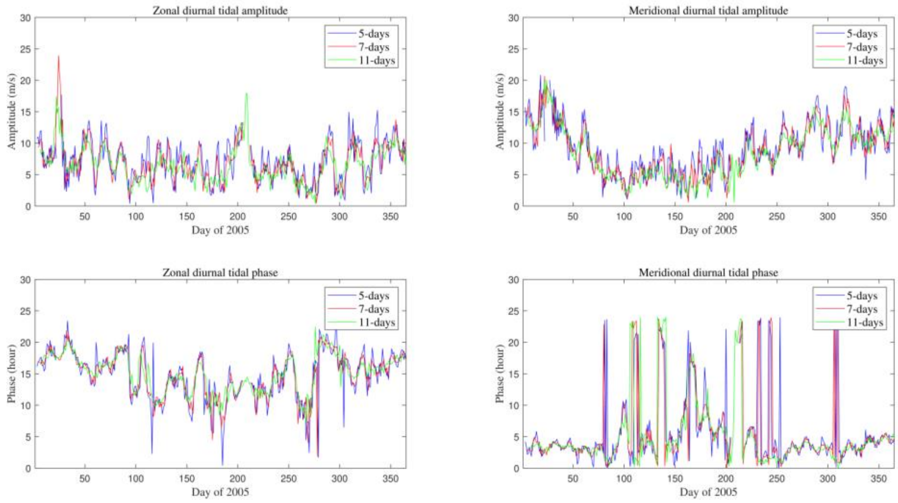

Figure A1. Zonal (left column) and meridional (right column) diurnal tide amplitudes (upper row) and phases (lower row) observed by the Svalbard Meteor Radar (SVMR) during 2005. The tidal amplitudes and phases are derived using sliding windows of 5 days (blue lines), 7 days (red lines), and 11 days (green lines).

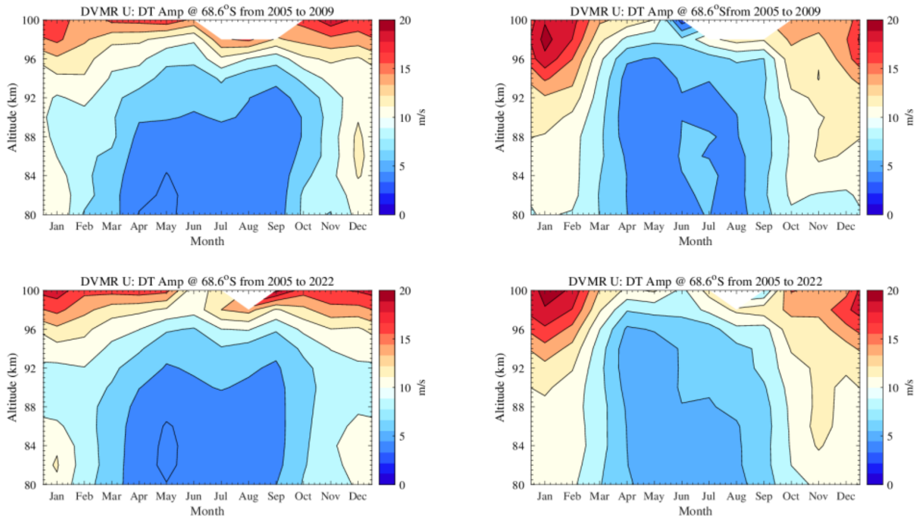

Figure A2. Zonal and meridional diurnal tide amplitude (left column) and phase (right column) observed by the Davis Meteor Radar (DVMR). Results derived from 2005–2022 are shown in the upper row, and those from 2005–2009 in the lower row.

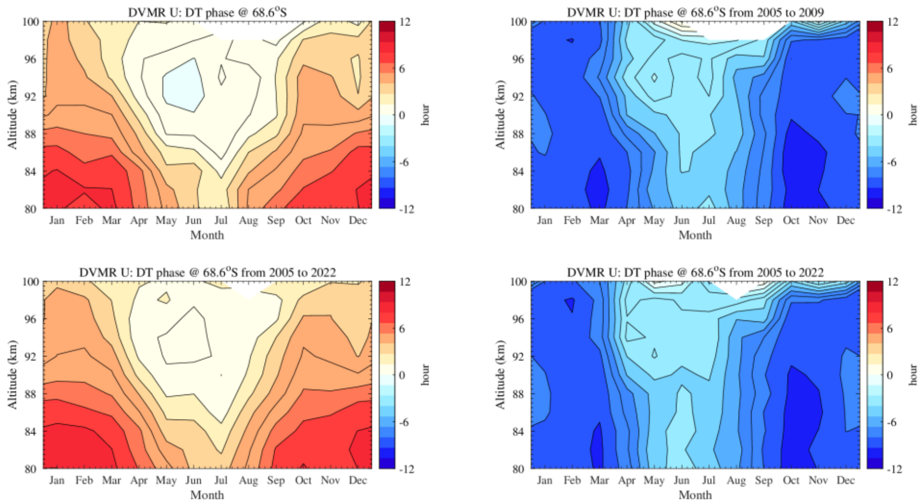

Figure A3. Same as A2, but for the meridional amplitude and phase.

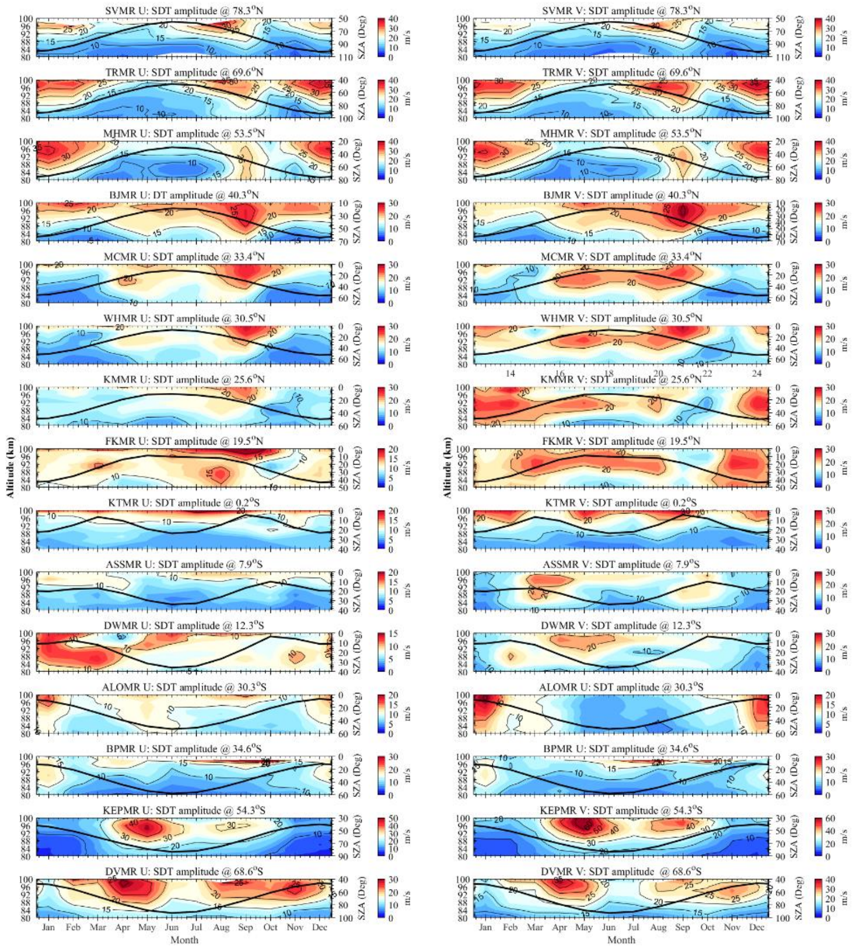

Figure A4. Monthly mean amplitudes of the composite zonal (U; left columns) and meridional (V; right columns) semidiurnal tidal (SDT) components derived from fifteen meteor radars. Note that the colorbar scales differ among panels. The black solid lines denote the solar zenith angle at local noon (1200 LT), shown on the right axes. The vertical black dashed lines indicate the spring and autumn equinoxes and the summer and winter solstices.

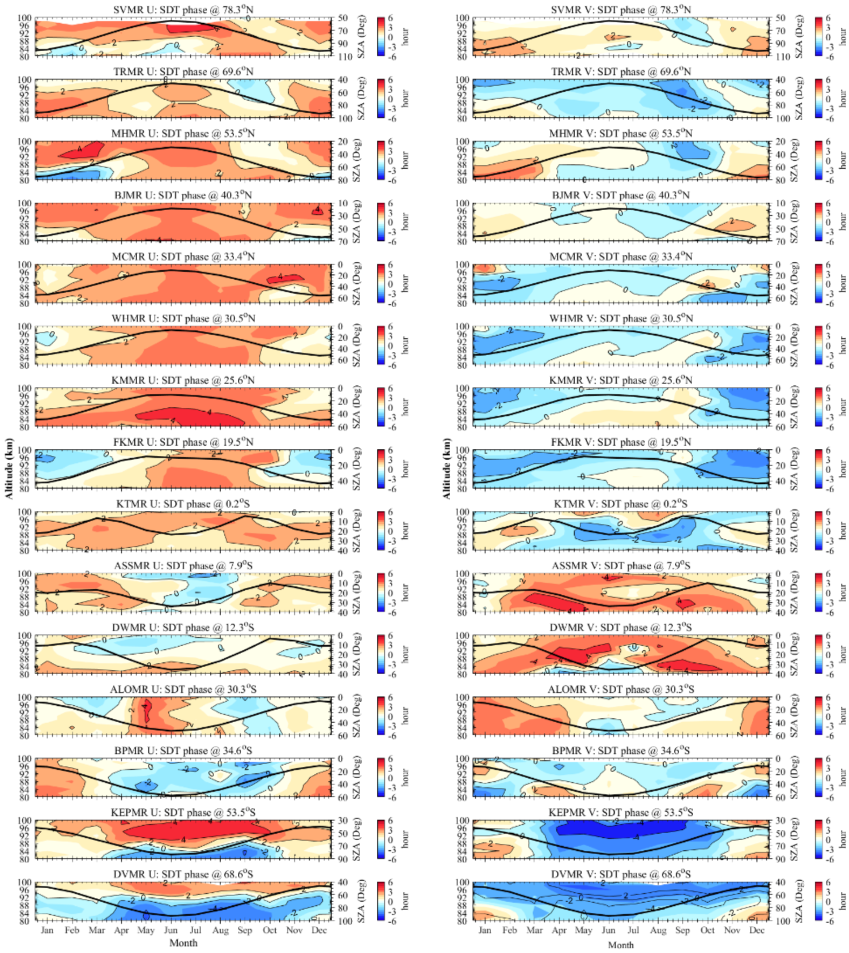

Figure A5. Same as Figure A4, but for the monthly mean phases of composite zonal (left column) and meridional (right column) semidiurnal tidal (SDT) components derived from fifteen meteor radars.

Data Availability Statement

The analyzed data presented in this manuscript are available at https://doi.org/10.6084/m9.figshare.29648918.v1 (Yi, 2025). The SD-WACCM dataset utilized in this study is available at https://doi.org/10.12176/01.60.00003-V01. The surface net solar radiation and surface latent heat flux data are available at at https://www.ecmwf.int/en/forecasts/dataset/ecmwf-reanalysis-v5.

Author contributions

Conceptualization: WY, XX; data curation: XX, IMR, RAV, AM, DJM, NG, MT, BN, GL, NJM, TMG, TT, AL, ZQ, JC, PPB and JC; formal analysis: WY, JYW and CY; funding acquisition: WY, XX, and JW; investigation: WY; methodology: WY and JYW; project administration: XX and WY; resources: WY and XX; software: WY and JYW; supervision: XX and WY; validation: WY and XX; visualization: WY; writing – original draft preparation: WY; and writing – review and editing:WY, JYW and DJM. All authors have read and agreed to the published version of the paper.

Acknowledgements

This work has been supported by the B-type Strategic Priority Program of CAS (grant no. XDB0780000); the National Natural Science Foundation of China (Grant 42125402, 42574213 and 42304165); the National Key Technologies R&D Program of China (Grant 2022YFF0503703); the Chinese Meridian Project; the Fundamental Research Funds for the Central Universities; the State Key Laboratory of Environment Characteristics and Effects for Near-space (No.2025NS02); the Joint Open Fund of National Field Observation and Research Station (Anhui Mengcheng) for Geophysics (MENGO-202602). This research was supported by the International Space Science Institute (ISSI) in Bern, through ISSI International Team project #23–580 “Meteors and phenomena at the boundary between Earth’s atmosphere and outer space”. The operation of the Davis meteor radar was supported by Australian Antarctic Science Projects 2668, 4025, 4445, and 4637. The publicly available dataset of CONDOR wind is supported by US NSF Grants 2432699 and 1828589. We acknowledge the effort from CONDOR team. The Svalbard meteor radar is supported by the Research Council of Norway under the project Svalbard Integrated Arctic Earth Observing System—Infrastructure development of the Norwegian node (SIOS-InfraNor, Project No. 269927).

References

Alexander, M. J., and H. Teitelbaum (2011) Three-dimensional properties of Andes mountain waves observed by satellite: A case study, J. Geophys. Res., 116, D23110, doi:10.1029/2011JD016151.

Becker, E., 2017: Mean-Flow Effects of Thermal Tides in the Mesosphere and Lower Thermosphere. J. Atmos. Sci., 74, 2043–2063, https://doi.org/10.1175/JAS-D-16-0194.1.

Cao, B., C. J. Heale, Y. Guo, A. Z. Liu, and J. B. Snively (2016), Observation and modeling of gravity wave propagation through reflection and critical layers above Andes Lidar Observatory at Cerro Pachón, Chile, J. Geophys. Res. Atmos., 121, 12,737–12,750, doi:10.1002/2016JD025173.

Cen, Y. (2022). 1979–2014 SDWACCM data [Dataset]. Figshare. https://doi.org/10.6084/m9.figshare.19777918

Chapman, S., Lindzen, R.S. (1970). Atmospheric tides: thermal and gravitational. Gordon and Breach, New York, NY, 200 pp.

Das S S, Kumar K K, Ramkumar G. (2013). First observations of quasi 120 day oscillation in mesospheric winds and temperature: Observations inferred from meteor radar. Radio Sci., 48: 310–315.

Devara, P. C. S., Ahmed, M. I. (1986). Momentum flux variations at lower thermospheric levels as seen from mid-latitude meteor wind observations. Meteorl. Atmos. Phys. 35, 236–241. https://doi.org/10.1007/BF01041816.

Davis, R. N., Du, J., Smith, A. K., Ward, W. E., and Mitchell, N. J. (2013). The diurnal and semidiurnal tides over Ascension Island (8 ° S, 14 ° W) and their interaction with the stratospheric quasi-biennial oscillation: studies with meteor radar, eCMAM and WACCM, Atmos. Chem. Phys., 13, 9543–9564, https://doi.org/10.5194/acp-13-9543-2013.

Deepa, V., Ramkumar, G., Antonita, M., Kumar, K. K. (2008). Meteor wind radar observations of tidal amplitudes over a low-latitude station Trivandrum (8.5 °N, 77 °E): Interannual variability and the effect of back ground wind on diurnal tidal amplitudes. J. Atmos. Sol.-Terr. Phys. 70: 2005-2013.

Forbes, J. M., and Garrett, H. B. (1979). Theoretical Studies of Atmospheric Tides. Rev. Geophys. Space Phys., 17, 1951-1981.

Forbes, J. M. Johnson, R. M. & Killeen, T. L. (Eds.) Tidal and Planetary Waves. The Upper Mesosphere and Lower Thermosphere: A Review of Experiment and Theory, American Geophysical Union, 1995, 67-87.

Guharay A, Batista P P, Buriti R A. (2021). Observations of a quasi-90-day oscillation in the MLT winds and tides over an equatorial station using meteor radar winds. Advances in Space Research, 67(10): 3125–3133.

Hagan, M. E., Burrage, M. D., Forbes, J. M., Hackney, J., Randel, W. J., Zhang, X. (1999). GSWM-98: Results for migrating solar tides. J Geophys Res., 104(A4), 6813–6827, doi:10.1029/1998JA900125.

Hagan, M. E., and Forbes, J. M. (2002). Migrating and nonmigrating diurnal tides in the middle and upper atmosphere excited by tropospheric latent heat release. J. Geophys. Res., 107(D24), ACL 6-1–ACL 6-15. https://doi.org/10.1029/2001JD001236.

Hagan, M. E., and Forbes, J. M. (2003). Migrating and nonmigrating semidiurnal tides in the upper atmosphere excited by tropospheric latent heat release. J. Geophys. Res., 108, A2, 1062, doi:10.1029/2002JA009466.

He, M., Chau, J. L., Stober, G., Li, G., Ning, B., & Hoffmann, P. (2018). Relations between semidiurnal tidal variants through diagnosing the zonal wavenumber using a phase differencing technique based on two ground-based detectors. Journal of Geophysical Research: Atmospheres, 123, 4015–4026. https://doi.org/10.1002/2018JD028400.

He, M., & Chau, J. L. (2019). Mesospheric semidiurnal tides and near-12 h waves through jointly analyzing observations of five specular meteor radars from three longitudinal sectors at boreal midlatitudes. Atmospheric Chemistry and Physics, 19(9), 5993–6006. https://doi.org/10.5194/acp-19-5993-2019.

Hersbach, H., Bell, B., Berrisford, P., et al. (2020). The ERA5 global reanalysis. Quarterly Journal of the Royal Meteorological Society, 146, 1999–2049. https://doi.org/10.1002/qj.3803.

Hindley N P, Mitchell N J, Cobbett N, et al. (2022). Radar observations of winds, waves and tides in the mesosphere and lower thermosphere over South Georgia island (54 °S, 36 °W) and comparison with WACCM simulations. Atmospheric Chemistry and Physics, 22 (14): 9435–9459.

Hocking, W. K., Fuller, B., & Vandepeer, B. (2001). Real-time determination of meteor-related parameters utilizing modem digital technology. Journal of Atmospheric and Solar-Terrestrial Physics, 63(2–3), 155–169. https://doi.org/10.1016/s1364-6826(00)00138-3.

Holdsworth, D. A., I. M. Reid, and M. A. Cervera (2004), Buckland Park all-sky interferometric meteor radar, Radio Sci., 39, RS5009, doi:10.1029/2003RS003014.
Huang, F. T., H. G. Mayr, C. A. Reber, T. Killeen, J. Russell, M. Mlynczak, W. Skinner, and J. Mengel (2006), Diurnal variations of temperature and winds inferred from TIMED and UARS measurements, J. Geophys. Res., 111, A10S04, doi:10.1029/2005JA011426.
Isoda, F., Tsuda, T., Nakamura, T., Vincent, R. A., Reid, I. M., Achmad, E., Sadewo, A., and Nuryanto, A. (2004). Intraseasonal oscillations of the zonal wind near the mesopause observed with medium-frequency and meteor radars in the tropics, J. Geophys. Res., 109, D21108, https://doi.org/10.1029/2003JD003378.
Jacobi, Ch., Portnyagin, Yu., Solovjova, T., et al., 1999. Climatology of the semidiurnal tide at 52°N–56°N from ground-based radar wind measurements 1985–1995. J Atmos Solar-Terr Phys., 61, 975–991.
Lieberman, R. S., D. A. Ortland, and E. S. Yarosh, Climatology and interannual variability of diurnal water vapor heating, J. Geophys. Res., 108(D3), 4123, doi:10.1029/2002JD002308, 2003.
Lieberman, R. S., D. M. Riggin, D. A. Ortland, S. W. Nesbitt, and R. A. Vincent (2007), Variability of mesospheric diurnal tides and tropospheric diurnal heating during 1997–1998, J. Geophys. Res., 112, D20110, doi:10.1029/2007JD008578.
Liu, A.& Franke, S. (2020). SKiYMET Meteor Radar Horizontal Wind [Dataset]. Zenodo. https://doi.org/10.5281/zenodo.4267128
Li, T., She, C. Y., Liu, H., Yue, J., Nakamura, T., and Krueger, D. A. (2009). Observation of local tidal variability and instability, along with dissipation of diurnal tidal harmonics in the mesopause region over Fort Collins, Colorado (41∘ N, 105∘ W), J. Geophys. Res.-Atmos., 114, D06106, https://doi.org/10.1029/2008jd011089.
Liu, G., Janches, D., Lieberman, R. S., Moffat-Griffin, T., Fritts, D. C., & Mitchell, N. J. (2020). Coordinated observations of 8-and 6-hr tides in the mesosphere and lower thermosphere by three meteor radars near 60°S latitude. Geophysical Research Letters, 47, e2019GL086629. https://doi.org/10.1029/2019GL086629.
Liu, H. L. and Hagan, M. E. (1998). Local heating/cooling of the mesosphere due to gravity wave and tidal coupling, Geophys. Res. Lett., 25, 2941–2944, https://doi.org/10.1029/98GL02153.
Liu, H., Tsutsumi, M., & Liu, H. (2019). Vertical structure of terdiurnal tides in the Antarctic MLT region: 15-year observation over Syowa (69∘S, 39∘E). Geophysical Research Letters, 46. https://doi.org/10.1029/2019GL082155
Liu, M., Xu, J., Liu, H., and Liu, X. (2016). Possible modulation of migrating diurnal tide by latitudinal gradient of zonal wind observed by SABER/TIMED. Sci. China Earth Sci. 59, 408–417 https://doi.org/10.1007/s11430-015-5185-4.
Llamedo, P., Salvador, J., de la Torre,A., Quiroga, J., Alexander, P., Hierro,R., et al. (2019). 11 years of Rayleigh lidar observations of gravity wave activity above the southern tip of South America. Journal of Geophysical Research: Atmospheres, 124, 451–467.https://doi.org/10.1029/2018JD028673.
Kishore Kumar, G., Singer, W., Oberheide, J., Grieger, N., Batista, P.P., Riggin, D.M., Schmidt, H., Clemesha, B.R. (2014). Diurnal tides at low latitudes: radar, satellite,

and model results. J. Atmos. Sol. Terr. Phys. 118, 96–105. http://dx.doi.org/10.1016/j.jastp.2013.07.005.

Kubota, M., A. Kano, H. Muramatsu, and H. Tomita, 2003: Intercomparison of Various Surface Latent Heat Flux Fields. J. Climate, 16, 670–678, https://doi.org/10.1175/1520-0442(2003)016<0670:IOVSLH>2.0.CO;2.

Manson, A. H., Meek, C.E., Hagan, M., et al. (1999). Seasonal variations of the semi-diurnal tides in the MLT: multi-year MF radar observations from 2 to 70 °N, and the GSWM tidal model. J Atmos Sol-Terr Phys., 61, 809–828.

Manson, A. H., C. M., M. Hagan, J. Koshyk, S. Franke, D. Fritts, C. Hall, W. Hocking, K. Igarashi, J. MacDougall, D. Riggin, and R. Vincent (2002). "Seasonal variations of the semi-diurnal and diurnal tides in the MLT: multi-year MF radar observations from 2-70 °N, modelled tides (GSWM, CMAM)." Ann. Geophys. 20: 661-677.

Manson, A. H., C. Meek, M. Hagan, X. Zhang, and Y. Luo (2004), Global distributions of diurnal and semidiurnal tides: Observations from HRDIUARS of the MLT region and comparison with GSWM-02 (migrating, nonmigrating components), Ann. Geophys., 22(5), 1529– 1548.

Manson, A. H., Meek, C. E., Chshyolkova, T., et al., (2009). Arctic tidal characteristics at Eureka (80 °N, 86 °W) and Svalbard (78 ° N, 16 ° E) for 2006/07: seasonal and longitudinal variations, migrating and non-migrating tides. Ann. Geophys., 27, 1153–1173, doi:10.5194/angeo-27-1153-2009.

McLandress, C., 2002a: The Seasonal Variation of the Propagating Diurnal Tide in the Mesosphere and Lower Thermosphere. Part I: The Role of Gravity Waves and Planetary Waves. J. Atmos. Sci., 59, 893–906, https://doi.org/10.1175/1520-0469(2002)059<0893:TSVOTP>2.0.CO;2.

McLandress, C., 2002b: The Seasonal Variation of the Propagating Diurnal Tide in the Mesosphere and Lower Thermosphere. Part II: The Role of Tidal Heating and Zonal Mean Winds. J. Atmos. Sci., 59, 907 - 922, https://doi.org/10.1175/15200469(2002)059<0907:TSVOTP>2.0.CO;2

Mitchell,N. J., Pancheva, D., Middleton, H., Hagan, M. (2002). Mean winds and tides in the Arctic mesosphere/lower thermosphere region and comparison with the GSWM. J Geophys Res., 106(A1), doi:10.1029/2001JA900127.

Mitchell, N. (2019). University of bath: Ascension Island Skiymet Meteor radar data (2005-2012) [dataset]. Centre for Environmental Data Analysis. https://catalogue.ceda.ac.uk/uuid/0d05cf74e17f49c2b7c5cd02faa59291.

Mitchell, N. (2021). University of bath: King Edward point Skiymet Meteor radar data (2016-2020) [dataset]. https://doi.org/10.5285/061fc7fd1ca940e7ad685daf146db08f.

Mukhtarov, P., Pancheva, D., and Andonov, B. (2009). Global structure and seasonal and interannual variability of the migrating diurnal tide seen in the SABER/TIMED temperatures between 20 and 120 km. J. Geophys. Res., 114(A2), A02309. https://doi.org/10.1029/2008JA013759

Murphy, D. J. (2003). Observations of a nonmigrating component of the semidiurnal tide over Antarctica. Journal of Geophysical Research, 108(D8), 4241. https://doi.org/10.1029/2002JD003077

Murphy, D. J., Forbes, J. M., Walterscheid, R. L., Hagan, M. E., Avery, S. K., Aso, T., et al. (2006). A climatology of tides in the Antarctic mesosphere and lower thermosphere. Journal of Geophysical Research, 111, D23104. https://doi.org/10.1029/2005JD006803

Oberheide, J., Wu, Q., Killeen, T. L., Hagan, M. E., & Roble, R. G. (2006). Diurnal nonmigrating tides from TIMED Doppler interferometer wind data: Monthly climatologies and seasonal variations. Journal of Geophysical Research, 111, A10S03. https://doi.org/10.1029/2005JA011491

Pancheva, D., Mukhtarov, P., Andonov, B., (2009). Global structure, seasonal and interannual variability of the migrating semidiurnal tide seen in the SABER/TIMED temperatures (2002– 2007). Ann Geophys., 27, 687–703.

Pancheva, D., P. Mukhtarov, and B. Andonov (2010), Climatology of the eastward propagating tides seen in the SABER/TIMED temperatures (2002–2007), Adv. Space Res., 46, 257–274, doi:10.1016/j.asr.2010.03.026

Pancheva, D., P. Mukhtarov, and A. K. Smith (2014), Nonmigrating tidal variability in the SABER/TIMED mesospheric ozone, Geophys. Res. Lett., 41, 4059–4067, doi:10.1002/2014GL059844.

Pancheva, D., Mukhtarov, P., Hall, C., Meek, C., Tsutsumi, M., Pedatella, N., Nozawa, S., Manson, A. (2020). Climatology of the main (24-h and 12-h) tides observed by meteor radars at Svalbard and Tromsø: Comparison with the models CMAM-DAS and WACCM-X, Journal of Atmospheric and Solar-Terrestrial Physics, doi: https://doi.org/10.1016/j.jastp.2020.105339.

Ramesh, K., Mitchell, N. J., Hindley, N. P., & Moffat-Griffin, T. (2024). Long-term variability and tendencies in mesosphere and lower thermosphere winds from meteor radar observations over Esrange (67.9°N, 21.1°E). Journal of Geophysical Research: Atmospheres, 129, e2023JD040404. https://doi.org/10.1029/2023JD040404.

Randall, C. E., et al. (2017), New AIM/CIPS global observations of gravity waves near 50–55 km, Geophys. Res. Lett., 44,7044–7052, doi:10.1002/2017GL073943.

Reid, I. M., McIntosh, D. L., Murphy, D. J., & Vincent, R. A. (2018). Mesospheric radar wind comparisons at high and middle southern latitudes. Earth, Planets and Space, 70(1), 84. doi:10.1186/s40623-018-0861-1.

Rienecker, M. M., Suarez, M. J., Todling, R., Bacmeister, J., Takacs, L., Liu, H., Gelaro, R. (2008). The GEOS-5 data assimilation system-documentation of versions 5.0.1, 5.1.0, and 5.2.0 (Vol. 27; Tech. Rep.). Technical Report Series on Global Modeling and Data Assimilation NASA/TM-2008-104606.

Riggin, D.M., Fritts, D.C., Jarvis, M.J., Jones, G., 1999. Spatial structure of the 12-hour wave in the Antarctic as observed by radar. Earth, Planets Space, 51, 621–628.

Sheng Z., He Y., Wang S., et al. (2025). Dynamics, chemistry, and modeling studies in the aviation and aerospace transition zone. The Innovation 6:101012.

Smith, A., 2012. Global dynamics of the MLT. Surv Geophys., 33, 1177–1230, doi: 10.1007/s10712- 012-9196-9.

Stober G, Kuchar A, Pokhotelov D, et al. (2021a). Interhemispheric differences of mesosphere–lower thermosphere winds and tides investigated from three whole-atmosphere models and meteor radar observations. Atmospheric Chemistry and Physics, 21 (18): 13855–13902.

Stober G, Janches D, Matthias V, et al. (2021b). Seasonal evolution of winds, atmospheric tides, and Reynolds stress components in the Southern Hemisphere mesosphere–lower thermosphere in 2019. Annales Geophysicae, 39 (1): 1–29.

Stober, G., Liu, A., Kozlovsky, A., Qiao, Z., Kuchar, A., Jacobi, C., Meek, C., Janches, D., Liu, G., Tsutsumi, M., Gulbrandsen, N., Nozawa, S., Lester, M., Belova, E., Kero, J., and Mitchell, N.: Meteor radar vertical wind observation biases and mathematical debiasing strategies including the 3DVAR+DIV algorithm, Atmos. Meas. Tech., 15, 5769–5792, https://doi.org/10.5194/amt-15-5769-2022, 2022.

Wang, J., Yi, W., Wu, J., Chen, T., Xue, X., Zeng, J., et al. (2022). Coordinated observations of migrating tides by multiple meteor radars in the equatorial mesosphere and lower thermosphere. Journal of Geophysical Research: Space Physics, 127, e2022JA030678. https://doi.org/10.1029/2022JA030678.

Wu, Q., D. A. Ortland, T. L. Killeen, R. G. Roble, M. E. Hagan, H.-L. Liu, S. C. Solomon, J. Xu, W. R. Skinner, and R. J. Niciejewski (2008a), Global distribution and interannual variations of mesospheric and lower thermospheric neutral wind diurnal tide: 1. Migrating tide, J. Geophys. Res., 113, A05308, doi:10.1029/2007JA012542.

Wu, Q., D. A. Ortland, T. L. Killeen, R. G. Roble, M. E. Hagan, H.-L. Liu, S. C. Solomon, J. Xu, W. R. Skinner, and R. J. Niciejewski (2008b), Global distribution and interannual variations of mesospheric and lower thermospheric neutral wind diurnal tide: 2. Nonmigrating tide, J. Geophys. Res., 113, A05309, doi:10.1029/2007JA012543.

Vincent, R. A., Kovalam, S., Fritts, D. C., and Isler, J. R. (1998). Long-term MF radar observations of solar tides in the low-latitude mesosphere: Interannual variability and comparisons with the GSWM. J. Geophys. Res., 103(D8), 8667–8683. https://doi.org/10.1029/98JD00482.

Xu, J., Smith, A. K., Liu, H.-L., Yuan, W., Wu, Q., Jiang, G., et al. (2009). Seasonal and quasi-biennial variations in the migrating diurnal tide observed by Thermosphere, Ionosphere, Mesosphere, Energetics and Dynamics (TIMED). Journal of Geophysical Research, 114, D13107. https://doi.org/10.1029/2008JD011298.

Yi, W., Xue, X. H., Chen, J. S., Chen, T. D., and Li, N. (2019). Quasi-90-day oscillation observed in the MLT region at low latitudes from the Kunming meteor radar and SABER. Earth Planet. Phys., 3(2), 1–11. http://doi.org/10.26464/epp2019013.

Yi W, Xue X H, Zeng J, et al. Observation of MLT region winds and tides by the USTC Mengcheng meteor radar. JUSTC, 2023, 53(5): 0501. DOI: 10.52396/JUSTC-2022-0158

Yi, Wen (2025). Monthly mean amplitudes and phases of composite zonal and meridional diurnal, semidiurnal and terdiurnal tidal components. figshare. Dataset. https://doi.org/10.6084/m9.figshare.29648918.v1

Zeng J, Yi W, Xue X, et al. (2022). Comparison between the mesospheric winds observed by two collocated meteor radars at low latitudes. Remote Sensing, 14 (10): 2354.

Zhang, R., X. Wang, and C. Wang, 2018: On the Simulations of Global Oceanic Latent Heat Flux in the CMIP5 Multimodel Ensemble. J. Climate, 31, 7111–7128, https://doi.org/10.1175/JCLI-D-17-0713.1.

Zhang, X., J. M. Forbes, and M. E. Hagan (2010), Longitudinal variation of tides in the MLT region: 2. Relative effects of solar radiative and latent heating, J. Geophys. Res., 115, A06317, doi:10.1029/2009JA014898.

Zhou, B. Z., Xue, X. H., Yi, W., Ye, H. L., Zeng, J., Chen, J. S., et al. (2022). A comparison of MLT wind between meteor radar chain data and SD-WACCM results. Earth and Planetary Physics, 6(5), 451–464. https://doi.org/10.26464/epp2022040.